Enhanced MODIS-derived ice physical properties within CoLM revealing bare ice-snow-albedo feedback over Greenland

删除[o_0 [2]]: MOIDS

Shuyang Guo[1], Yongjiu Dai[1]*, Hua Yuan[1], Hongbin Liang[1]

[1] Southern Marine Science and Engineering Guangdong Laboratory (Zhuhai), School of Atmospheric Science, Sun Yat-sen University, Zhuhai, China

Corresponding author: Yongjiu Dai (daiyj6@mail.sysu.edu.cn)

Submitted to *The Cryosphere*

Abstract

Under global warming, the Greenland Ice Sheet (GrIS) is experiencing unprecedented mass loss. One key contributing factor is the change in snow and ice albedo, which is closely related to firn metamorphism. To investigate the impact of bare ice microstructure changes on the regional warming of the GrIS ablation zone, SNICAR-ADv4 (Snow, Ice and Aerosol Radiation model Adding-Doubling Version 4), a physically based radiative transfer model, is incorporated in the Common Land Model version 2024 (CoLM2024). It allows the land surface model to represent the ice albedo with changes in ice properties rather than using a constant ice albedo value. Quality control was conducted on the bare ice physical property dataset input into CoLM, with multiple MODIS products combined to ensure accuracy. The application of SNICAR-ADv4 reduced the overestimation of shortwave broadband albedo by 38%, with a bias of 0.053. Further sensitivity experiments indicate that the summer albedo in the bare ice region is reduced by 0.032 due to the bare ice metamorphism, producing a 2-m temperature forcing of 0.071°C, a snow cover change of -0.011, and a snow water equivalent forcing of -1.345 mm. These changes lead to increased bare ice exposure, further reducing albedo and enhancing solar radiation absorption by the surface, thereby reinforcing a feedback involving bare ice, snow, and albedo. This highlights the critical role of bare ice physical properties in amplifying melt through the bare ice-snow-albedo feedback, with stronger feedbacks expected in a fully coupled land-atmosphere model.

删除[o_0 [2]]: only

删除[o_0]: under

Keywords

Greenland Ice Sheet; Bare ice region; Ice albedo; Albedo feedback; MODIS; Remote sensing

1. Introduction

The Greenland Ice Sheet (GrIS) has been melting at a rapid pace since the 1990s, losing around 255 Gt of ice annually in 2003-2016 (Sasgen et al., 2020; Li et al., 2022; van den Broeke et al., 2017). The decreasing mass balance of the GrIS and peripheral glaciers is the

删除[o_0 [2]]: , the last remnant of the Ice Age

删除[o_0 [2]]: negative

most significant cryospheric factor driving sea level rise, contributing over 25% of observed global sea level rise (Chen et al., 2017; Ryan et al., 2019). The total mass loss from GrIS consists of two components: surface runoff and frontal ablation occurring at the terminus of outlet glaciers (Cogley et al., 2011, Kochtitzky et al., 2023). Surface losses have exceeded dynamical losses in contributing to GrIS mass loss since 2000, with 55% of Greenland's total mass loss attributed to surface mass balance (SMB) and 45% to the discharge of outlet glaciers between 2000-2018 (Mouginot et al., 2019). These melting processes are driven by a combination of factors, including atmospheric warming, a reduced water retention capacity of firn due to densification, and a lower surface albedo (Hofer et al., 2017; King et al., 2020; Ryan et al., 2024).

删除[o_0 [2]]: Such melting was linked to a combination of processes including climate warming, reduced retention capacity of firn and lower surface albedo (Hofer et al., 2017; King et al., 2020; Ryan et al., 2024).

Ice melt on the surface of the GrIS is partially regulated by the surface albedo. It serves as a fundamental parameter in controlling the absorption of insolation by the ice sheet (Box et al., 2012; Naegeli et al., 2017, Feng et al., 2024). A minor change in snow and ice surface albedo can exert a substantial effect on the energy budget of the regional surface-air system, causing significant fluctuations in the energy flux on the surface of the GrIS (Nolin and Stroeve, 1997). Surfaces with high albedo, such as fresh snow, efficiently reflect solar radiation, whereas darker areas, such as glacier ice, absorb the majority of incoming shortwave energy (Whicker-Clarke et al., 2022). Snow and ice albedo varies with the spatial distribution of snow, ice, and biotic and abiotic light absorbing constituents (LACs) and further evolves with the melting of snowpack and glacier surfaces through the spring and summer. Fluctuations in the snowline dictate the relative extent of dark bare ice versus brighter snow (Ryan et al., 2019). These directly influence GrIS surface melt through the exposure of bare ice (Antwerpen et al., 2022) and the processes that darken bare ice itself (Chevrollier et al., 2023). Dark bare ice extent closely tracks interannual variations in snowline elevation and is exposed as the snowline retreats further inland during the melt season, leading to the reduction of ice sheet albedo and the intensified melt. This positive feedback has been referred to as the "snow-albedo feedback" (Ryan et al., 2019).

删除[o_0]: discharge

In the preceding decades, polar amplification has contributed to the progressive darkening of

the GrIS and the prolongation of the melt season, both of which serve as positive feedback mechanisms that intensify surface melt (Tedesco et al., 2016). As the warming occurs over the ice surface, bare ice albedo is reduced through melt processes that darken the ice surface. Notably, these processes include exposure of dust layers, pooling of surface meltwater, increased interstitial water content, and liquid meltwater-induced growth of pigmented ice algal assemblages that inhabit the bare ice surface (Cook et al., 2020; Stibal et al., 2017; Tedstone et al., 2020; Williamson et al., 2018; Whicker-Clarke et al., 2022). Despite operating over a relatively small area of the ice sheet, it is argued that these bare ice processes have contributed substantially to an observed reduction in albedo and associated increase in melt across GrIS's ablation zone from 2000 to 2011 (Stibal et al., 2017; Tedstone et al., 2017). This category of physical and biological melt-albedo processes that darken bare ice is referred as the "bare ice-albedo feedback" (Ryan et al., 2019). However, the complex and non-linear response of regional snow and ice, particularly in ablation zones, to changes in meteorology and climate highlights the growing necessity to model these surfaces using physical principles rather than relying solely on empirical methods (Box et al., 2012). Therefore, accurately modeling the influence of snow and ice on the albedo of the GrIS becomes increasingly important to capture these dynamics effectively.

The albedo of the cryosphere varies widely depending on the solar zenith angle (SZA), atmospheric conditions, metamorphic state of the snow and ice, and impurities (He and Flanner, 2020). The Snow, Ice, and Aerosol Radiative (SNICAR) model is one of the most widely used snowpack radiative transfer models (Flanner et al., 2021). Initially, it combined the theory from Wiscombe and Warren (1980) and Warren and Wiscombe (1980) with the multi-layer two-stream solution from Toon et al. (1989) to enhance the simulation of snow albedo (Flanner et al., 2007). Updates and new features have also been incorporated within SNICAR, including eight species of LACs (Flanner et al., 2007), four snow grain shapes (He et al., 2018), black carbon-snow and dust-snow internal mixing state (Flanner et al., 2012; He et al., 2017, 2019). Dang et al. (2019) developed SNICAR-AD by substituting the tri-diagonal matrix solution solving method (Toon et al., 1989) with the delta-Eddington adding-doubling radiative method, as a result of the latter's superior computational stability

across varying solar zenith angles and higher computational efficiency (He et al., 2024). To represent ice albedo, Whicker-Clarke et al. (2022) further developed SNICAR-ADv4 by integrating and extending key features from earlier radiative transfer models to achieve more accurate simulations of a spectrally resolved cryospheric column of snow and ice with a refractive boundary, while incorporating light-absorbing constituents (LACs), such as black carbon (BC) and algae, into this standalone radiative transfer model. It simulates bare ice using the physical microscopic structure of the ice, including the ice density, the scattering air bubbles within an absorbing ice medium, and a refractive boundary that depicts the refraction across snow-ice interfaces (Briegleb and Light, 2007; Gardner and Sharp, 2010; Mullen and Warren, 1988).

Nevertheless, the ice albedo is typically prescribed as constant values in the visible (VIS) and near-infrared (NIR) spectral regions in Earth system models. For instance, Ice albedo is 0.6 in the visible and 0.4 in the NIR in the default version of the Energy Exascale Earth System Model (E3SM) and the Community Earth System Model (CESM) version 2 (Whicker-Clarke et al., 2024). Prescribing constant albedo values does not represent the physical variability of solid ice albedo or its spectral changes under varying conditions. To advance ice radiative transfer modeling in Earth system models, Whicker-Clarke et al. (2024) incorporated SNICAR-ADv4 into the E3SM (specifically its land component, ELM), in which the GrIS ice physical properties are retrieved from the satellite observation data. This enhancement enables more realistic simulations of the GrIS bare ice albedo, and concurrently reveals that the default ELM method overestimates bare ice albedo by 4% in the visible and 7% in the NIR bands. However, the quality information of MODIS albedo products were not considered in the process of acquiring bare ice properties in their study. Schaaf et al. (2011) noted that the MODIS poor-quality inversions beyond a SZA of 70° are characterized by high noise and often significantly lower than the more stable and consistent values observed at smaller SZAs. Omitting quality flags could, therefore, lead to an underestimation of Greenland's snow/ice albedo and introduce significant uncertainties in the retrieval of bare ice physical properties. Despite the aforementioned modeling advances, the Common Land Model (CoLM) still uses fixed values to represent ice albedo (0.60 in the visible and 0.40 in

删除[o_0]: a

删除[o_0]: (ESMs)

删除[o_0 [2]]: Such parameterization does not capture the albedo of solid ice or variations in spectral albedo with changing ice conditions.

删除[o_0]: (ESMs)

删除[o_0]: by

the NIR). For the purpose of investigating the impacts of bare ice metamorphism under polar warming, it is also imperative to incorporate ice radiative transfer techniques into CoLM to enhance albedo modeling with more realistic and physical representations of snow-ice-LAC-radiation interactions.

In this study, we focus on the bare ice region of the GrIS, characterized by the presence of land ice, and bare ice is exposed by snow melting during the ablation season. The aim of this study is to develop a more reliable dataset of Greenland's bare ice physical properties by incorporating the quality information of MODIS albedo products, and explore the bare ice-albedo feedback associated with the metamorphism of bare ice after the implementation of the SNICAR-ADv4 into the CoLM. This paper is organized as follows. Section 2 provides descriptions of the CoLM snow and ice albedo schemes and details the model simulations, as well as the explanation of the use of various MODIS products to inform the ice albedo calculations in SNICAR-ADv4. Section 3 compares the differences in albedo simulations with and without ice radiative transfer solver (SNICAR-AD and SNICAR-ADv4), and quantifies the impact of varying bare ice properties on the near-surface air temperature and the snow cover. Section 4 is conclusions and discussion.

删除[o_0]: with

删除[o_0]: d

2. Models, Data, and Methods

2.1 Snow and Ice Albedo Schemes

This study utilizes two distinct implementations of the SNICAR model within the CoLM for snow and ice albedo simulations: (i) the baseline SNICAR-AD version (Dang et al., 2019) and (ii) the enhanced SNICAR-ADv4 version (Whicker-Clarke et al., 2024). Both versions adopt identical snow albedo algorithms but exhibit distinct ice albedo treatments. Specifically, as shown in Figs. 1a and b, the SNICAR-ADv4 accounts for radiative transfer through the ice column, while the SNICAR-AD prescribes ice albedo as constant values: 0.6 for visible (VIS: 0.3–0.7 μm) and 0.4 for near-infrared (NIR: 0.7–5.0 μm) bands. The snow albedo scheme of SNICAR-AD/SNICAR-ADv4 in the CoLM computes snow albedo for the multi-layer (up to

5 layers) snowpack with the two stream radiative transfer scheme of the delta-Eddington approximation and adding-doubling technique, accounting for the effects of snow properties (e.g., grain size and shape) and LAC contamination on snow albedo.

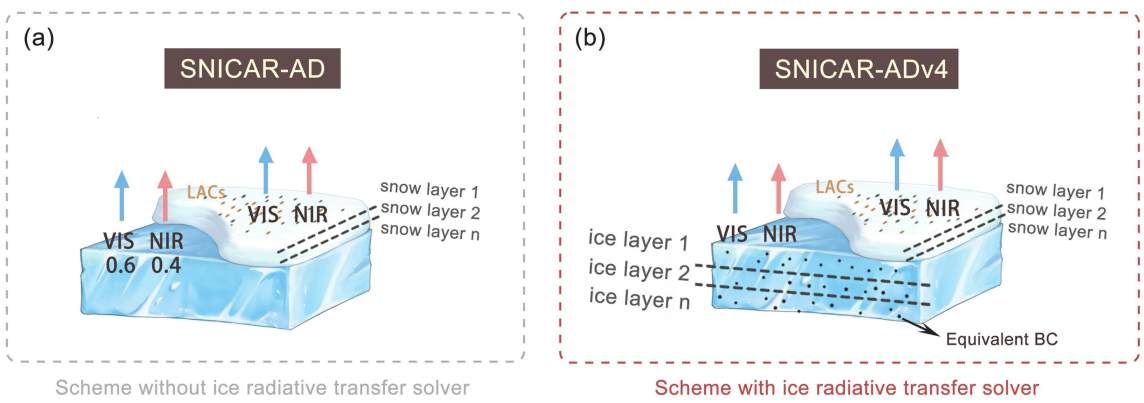

Figure 1. Schematic representation of the snow and land ice column in CoLM SNICAR-AD and SNICAR-ADv4.

For snow albedo simulation, the SNICAR-AD/SNIACR-ADv4 embedded in CoLM uses the physical properties of the snowpack and albedo of the top layer of the underlying ground to determine the column albedo (Flanner and Zender, 2006). The input variables consist of direct and diffuse radiation, the surface downward solar spectrum, the solar zenith angle (for direct radiation), the ground albedo beneath the snowpack, vertical profiles of snow grain size, snow layer thickness and density, aerosol concentrations of each snow layer, as well as the optical properties of both snow and aerosols. Meanwhile, parameterizations for snow grain shapes (sphere, spheroid, hexagonal plate, and Koch snowflake) and LACs-snow mixing states (BC/dust externally or internally mixed with snow grains) are included to improve the simulations of snow surface energy and water balances (Hao et al., 2023).

For ice albedo modeling, the advent of the SNICAR-ADv4 enables us to explore the regional climatic response induced by changes in ice albedo using the ice microphysical properties derived from satellite products. As proposed by Whicker-Clarke et al. (2024), the radiation transfer process within the ice layer can be calculated in the land surface model, which requires input variables such as ice density, air bubble effective radii within the ice,

equivalent BC concentrations, and downward solar spectra. The need for air bubble parameters arises from the representation of ice layers as collections of independently scattering air bubbles within a solid ice medium in SNICAR-ADv4, while snow layers are treated as independently scattering ice crystals in an air medium (Picard et al., 2016; Whicker-Clarke et al., 2022).

In addition to the albedo scheme, we briefly describe the physical processes represented by the glacier and snow modules in CoLM to clarify model capabilities. The glacier component is designed to capture essential surface thermodynamic processes, including full surface energy balance calculations and subsurface heat diffusion through a multi-layer ice column. However, it omits several key elements found in more advanced land ice schemes: (1) the model assumes fixed ice thickness and does not track accumulation or ablation, lacking mass-conserving SMB computation; (2) glacier geometry is static, with no coupling to an ice sheet model for dynamic evolution; and (3) meltwater generated from glacier ice is retained rather than routed to runoff, leading to unrealistic surface water storage. In contrast, the snow component in CoLM simulates several critical processes: (1) multi-layer snowpack energy and mass balance, including radiative, turbulent, and conductive heat fluxes; (2) vertical snow temperature evolution and phase changes; (3) melt, liquid water percolation, refreezing, sublimation and snowmelt runoff generation; and (4) snow aging and albedo evolution, with consideration of the impacts of LAPs, as represented by SNICAR-AD/SNICAR-ADv4.

2.2 Data

MODIS MCD12C1, MOD09CMG, and MOD10C1 products with consistent 0.05° spatial resolution were utilized for GrIS bare ice monitoring during the summer melt seasons of 2000-2020. The MCD12C1 Version 6.1 annual land cover type product (Friedl et al., 2010) provided initial cryospheric classification by excluding grids not categorized as snow or ice. The MOD09CMG (Vermote 2021) band 2 reflectance (0.841–0.876 μm) was employed for bare ice-snow discrimination, where pixels with reflectance values below 0.6 were classified as bare ice. Comparative spectral analysis of MODIS imagery by Shimada et al. (2016)

revealed markedly greater surface reflectance in snow-covered pixels relative to bare ice across all spectral bands, with maximal contrast observed at 0.86 μm. The robustness of this threshold was confirmed by Antwerpen et al. (2022) through comparison with Landsat 8 OLI (Operational Land Imager), showing a relative error of only 0.16% in bare-ice classification accuracy. The MOD10C1 product was further used to exclude pixels with cloud obstruction percentage exceeding 90% or snow cover fraction above 90% (Antwerpen et al., 2022; Whicker-Clarke et al., 2024). The derived bare ice extent was filtered by excluding pixels above the mean equilibrium line altitude of 1679 m a.s.l., defined as the 95th percentile of ablation zone elevations (Antwerpen et al., 2022). This conservative threshold minimizes sporadic high-elevation detections while maintaining robust estimation of the mean equilibrium line altitude (Antwerpen et al., 2022).

The MODIS MCD43C3 product (Schaaf et al., 2002) is used to retrieve bare ice physical properties by using standalone SNICAR-ADv4, and to evaluate CoLM-simulated albedo over the GrIS bare ice regions. This daily product provides spectral (MODIS bands 1 to 7) and broadband (VIS 0.3–0.7 μm, NIR 0.7–5.0 μm and shortwave 0.3–5.0 μm) black-sky albedo (BSA) and white-sky albedo (WSA) at local solar noon, derived from 16 days of Aqua-Terra merged surface albedo dataset based on the bidirectional reflectance distribution function (BRDF) algorithm (Schaaf and Wang, 2021). Compared with the GLASS-AVHRR and C3S-v2 albedo products, MCD43C3 demonstrates superior performance for monitoring snow albedo, exhibiting the lowest bias and RMSE over snow and consistent performance across diverse snow cover conditions (Urraca et al., 2022). In the GrIS, MCD43A3 was found to outperform the GLASS albedo product and even the reconstructed albedo based on the MOD10A1, for the sites located in the GrIS ablation zone (Ye et al., 2023). In this study, shortwave albedo under direct radiation is treated as equivalent to the BSA, in accordance with the widely accepted terminology used in the MCD43C3 product.

Considering the little difference between BSA and WSA for a typical summer day, using BSA is considered acceptable for analyzing the GrIS during the summer (Alexander et al., 2014; Stroeve et al., 2005). The extracted variables in this study from MODIS MCD43C3

设置格式[o_0 [2]]: 字体: （默认）Times New Roman

删除[o_0 [2]]: The robustness of this threshold was confirmed by Antwerpen et al. (2022) through comparison with Landsat 8 OLI (Operational Land Imager), with a relative error of 0.16%.

设置格式[o_0 [2]]: 字体: （默认）Times New Roman

删除[o_0 [2]]: Among the GLASS-AVHRR and C3S-v2 albedo products, MCD43C3 stands out as the most reliable for monitoring snow albedo, exhibiting the lowest bias and RMSE over snow and consistent performance across diverse snow cover conditions (Urraca et al., 2022).

include Band 2 BSA, broadband BSA (visible, near-infrared and shortwave), along with local noon solar zenith angles (SZAs) and albedo quality index. The MCD43C3 albedo quality index helps identify regions with cloud cover contamination, detrimental atmospheric conditions, or insufficient observational data. Figure 2a shows the daily variation of the regionally weighted average SZA over Greenland during May-September. The period with SZA>70° occurs primarily in September. For the relationship between the SZAs of MCD43C3 and their spatiotemporally corresponding albedo quality index (Fig. 2b), it can be seen that the percentage of low-quality indices (4 and 5) rises drastically as the SZA increases at higher SZA. To ensure reliable satellite-retrieved bare ice physical properties, we excluded all albedo values identified with a low-quality index (4 or 5), regardless of the SZA. Figure 2b shows that the proportion of low-quality indices increases markedly when the SZA exceeds 70°, indicating that such filtering primarily affects high-SZA retrievals.

删除[o_0 [2]]: Therefore, we excluded albedo values identified with a low-quality index when the SZA exceeded 70° to derive more reliable satellite-retrieved bare ice physical properties.

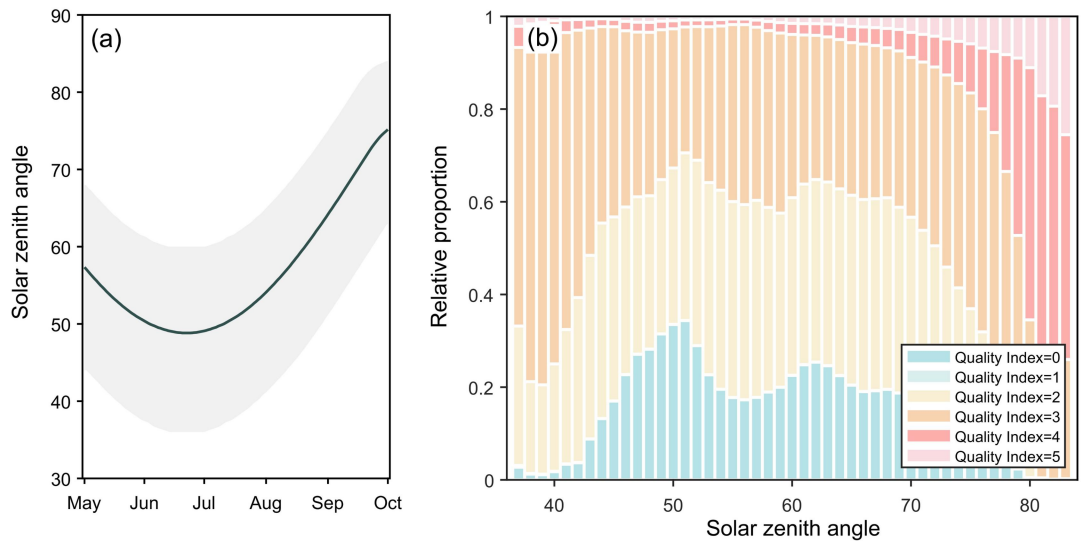

Figure 2. Regional-weighted mean SZAs of Greenland at local noon from May to September (a; solid line). Grey shaded area represents the range of SZAs over Greenland. Relative proportion of the quality index of MCD43C3 albedo dataset under different SZAs over Greenland during May to September (b; 0 for best quality and 5 for poorest quality)

2.3 Parameter sensitivity of ice spectral albedo in SNICAR-ADv4

We use the standalone SNICAR-ADv4 model to briefly examine the key factors influencing the spectral albedo of ice under direct illumination conditions. These factors include SZA, ice

density, air bubble effective radius (Reff), and black carbon (BC) concentration. This sensitivity analysis provides a foundation for the subsequent method of obtaining ice physical properties (Section 2.4). As shown in Fig. 3a, total internal reflection occurs at wavelengths around 3μm for SZA greater than 55°, and the wavelength range for total internal reflection expands with the increases in SZAs. This phenomenon occurs for pure and smooth ice surfaces but is not representative of naturally occurring ice, which typically has impurities and rough surfaces. For the dependency of albedo on ice density, and air bubble effective radius, the spectra show that the albedo declines as the ice density and air bubble radius increases since air bubbles within the ice are responsible for the scattering light and smaller bubbles scatter light more efficiently in the visible and near-infrared parts of the spectrum (Figs. 3b-c). Furthermore, BC impacts ice albedo rather uniformly across the visible spectrum and has almost no impact at $\lambda > 1.0$ μm (Fig. 3d).

删除[o_0]: ，

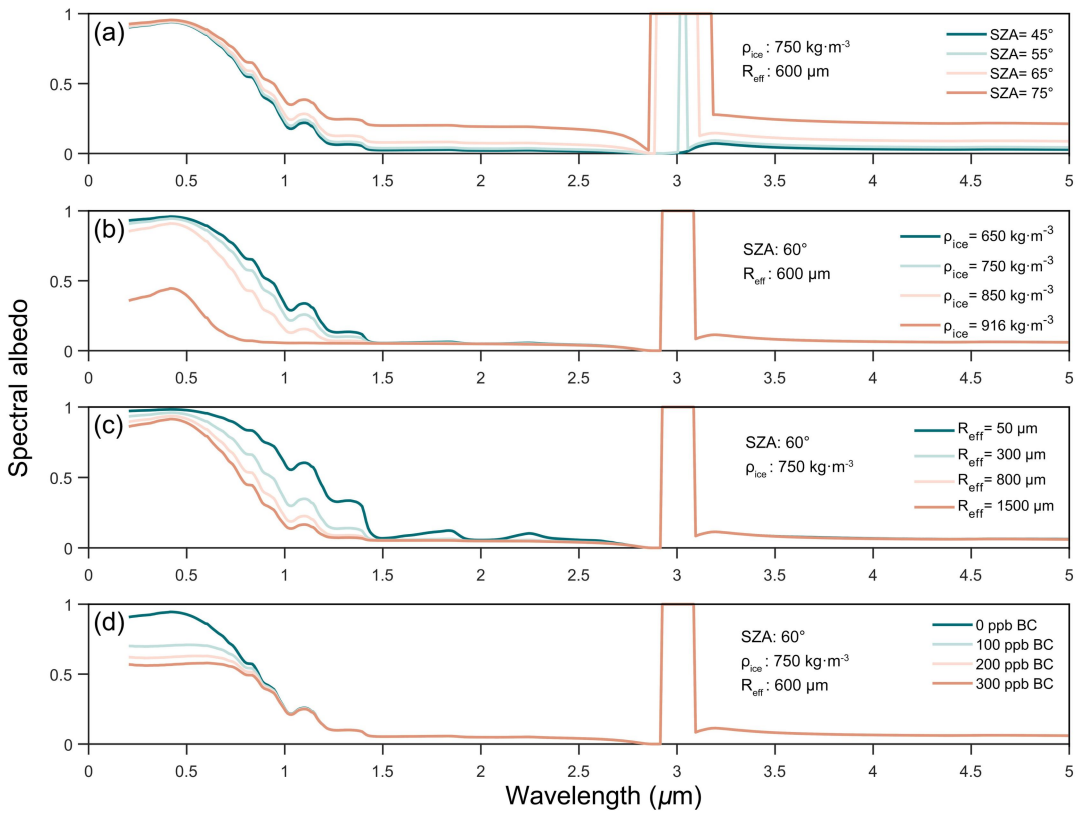

Figure 3. Spectral albedo simulated by standalone SNICAR-ADv4 under direct incident irradiance with varing (a) SZA, (b) ice density, (c) air bubble effective radius and (d) BC concentration.

While these controlled simulations clarify the fundamental optical behavior of ice under idealized conditions, natural environments involve more complex interactions shaped by microstructural evolution and meteorological forcing. A synthetic description of bare ice metamorphism includes the evolution of air bubbles and density: newly fallen snow starts with low density and open pore spaces, which become compacted through wind-driven grain fragmentation and rounding, forming wind slabs. Further densification occurs via grain-boundary sliding and pressure-induced deformation, during which air bubbles become sealed and gradually shrink under compression (Tedesco et al., 2016). In ablation zones, these densification processes are coupled with surface metamorphism. Glaciers undergoing melt often develop a porous weathering crust composed of loosely interlocked crystals, formed by differential solar absorption along grain boundaries, a process termed internal ablation (Müller and Keeler, 1969). Under overcast, windy, and warm conditions, this crust is preferentially removed, exposing denser, glazed ice beneath. Temperature-driven grain sintering and densification further reduce SSA by smoothing and coalescing ice grains (Flanner and Zender, 2006; Hofer et al., 2017). Concurrently, air bubble growth from differential solar heating and subsurface melting continues to modify the microstructure and optical properties of the ice.

2.4 Method

The method for obtaining ice physical properties (ice density, air bubble effective radius and equivalent BC) from MODIS bare ice albedo involves two main steps (Whicker-Clarke et al., 2024). First, as detailed in Section 2.2, bare ice spatiotemporal distribution was determined through the integrated use of MODIS products, employing MCD12C1 to exclude non-cryospheric pixels, MOD09CMG to distinguish bare ice from snow cover, and MOD10C1 to apply snow and cloud masking. Second, the bare ice physical properties (ice density and air bubble effective radius) are retrieved using the physical properties and SZA within the precomputed standalone SNICAR-Adv4 lookup table to match MCD43A3 band 2 BSA. Notably, this step derives only ice density and air bubble effective radius, whereas equivalent BC concentration requires additional processing steps described later in this

删除[o_0 [2]]: Second, the bare ice physical properties (ice density and air bubble effective radius) are retrieved using MCD43A3 band 2 BSA and its corresponding SZA to match the closest physical properties within the precomputed lookup table by standalone SNICAR-ADv4 model.

删除[o_0 [2]]: black carbon (

删除[o_0 [2]]:)

section. After obtaining all bare ice physical properties (ice density, air bubble effective radius, and equivalent BC concentration), we upscaled the data from a spatial resolution of 0.05°×0.05° to 0.5°×0.5°.

The lookup table was generated using the standalone SNICAR-ADv4 radiative transfer model by testing a range of parameter combinations within physically constrained ranges, including ice density (650-916 $kg \cdot m^{-3}$) and air bubble radii (100-1500 μm), as well as the SZAs spanning 35° to 75° to represent typical local noon conditions across the GrIS grid cells. Following the SNICAR-ADv4 modeling configuration, ice with densities above 650 $kg \cdot m^{-3}$ is treated as bubbly ice, following the modeling approach in Whicker-Clarke et al. (2022), which showed optimal agreement with in situ measurements. However, because the density-bubble radius relationship for GrIS bare ice remains poorly constrained, we apply a linear density-radius relationship as a first-order approximation for calculating the specific surface area (SSA), where densities of 650 $kg \cdot m^{-3}$ and 916 $kg \cdot m^{-3}$ correspond to bubble radii of 50 μm and 1500 μm, respectively (Fig. 4a). This parameterization is provisional and awaits future observational validation. For each parameter combination, the band 2 albedo, SSA and the volume fraction of air (V_{air}) were then output by the standalone SNICAR-ADv4. The SSA is a measure of the total surface area of ice-air interfaces relative to the ice mass. The relationship between the SSA (units: $m^2 \cdot kg^{-1}$) and ice density and air bubble effective radius is given by Eq.1, where ρ_{blk} is layer bulk ice density used to calculate the volume fraction of air (Eq.2).

$$SSA = \frac{3V_{air}}{\rho_{blk} R_{eff}} \quad (1)$$

$$V_{air} = \frac{\rho_{ice} - \rho_{blk}}{\rho_{ice}} \quad (2)$$

Figure 4b shows the band 2 albedo from the SNICAR-ADv4 lookup table as a function of SSA, illustrating that the modeled albedo is primarily determined by SSA rather than the specific combination of ice density and bubble size. Consequently, the retrieval algorithm selects the (density, radius) combination that most closely reproduces the observed Band 2 albedo. Since MCD43C3 provides the band 2 albedo and SZA for each bare ice grid cell, the corresponding bare ice physical properties can be inferred from the lookup table. It is

删除[o_0 [2]]: Ice with densities above 650 $kg \cdot m^{-3}$ is conventionally classified as cryospheric media, consistent with in situ measurements (Whicker-Clarke et al., 2022)

删除[o_0 [2]]: ing

删除[o_0 [2]]: 3

删除[o_0 [2]]: α,

删除[o_0 [2]]: <math>

删除[o_0]: Eq.

删除[o_0]: Eq.

删除[o_0 [2]]: 3

337 important to note, however, that the resulting bare ice property maps (Figs. 4c-f) represent
338 just one plausible solution among several combinations that could yield similar SSA and
339 albedo values.

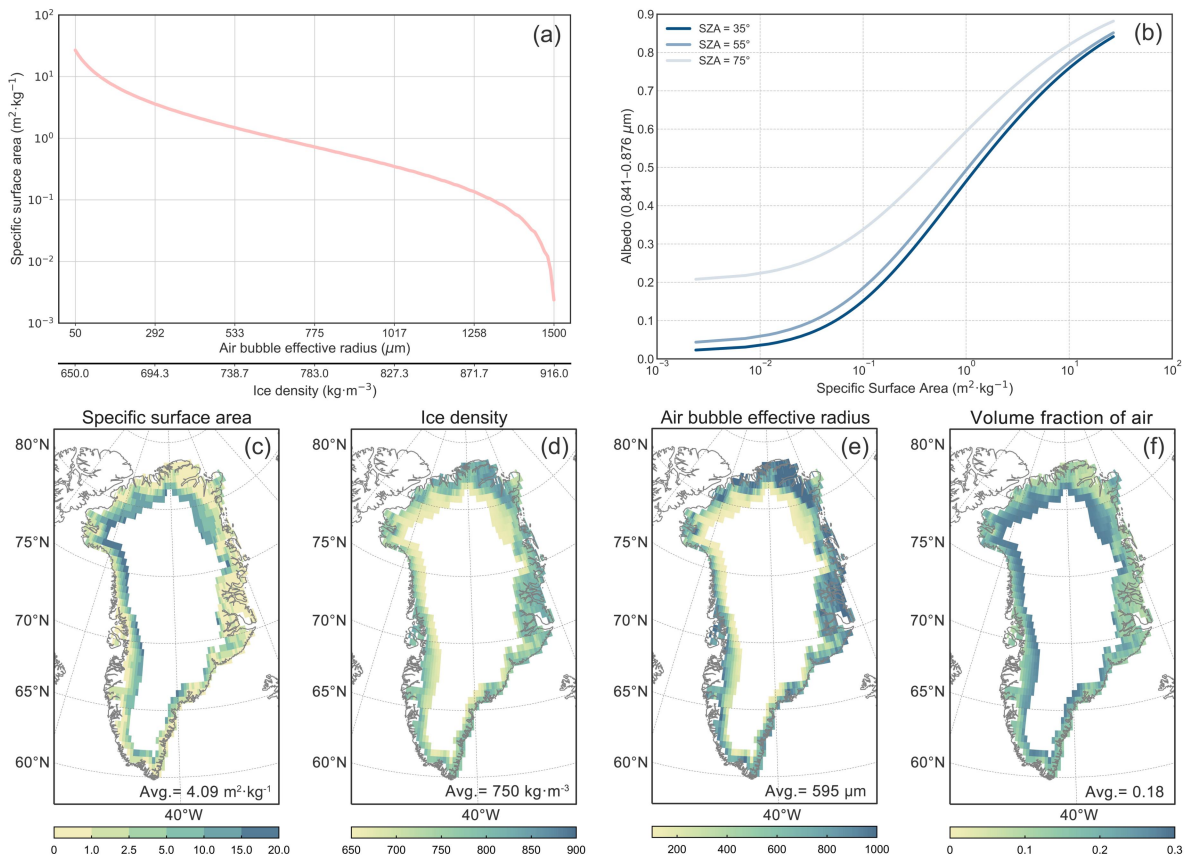

340

341 **Figure 4.** The relationship between ice specific surface area (SSA; $m^2 \cdot kg^{-1}$), air bubble
342 effective radius (μm) and ice density ($kg \cdot m^{-3}$) under a linear density-radius relationship (a
343 first-order approximation) assumed in this study (a). MCD43C3 band 2 (0.841-0.876 μm)
344 albedo as a function of SSA and solar zenith angle (b). Spatial distribution of JJA (c) specific
345 surface area ($m^2 \cdot kg^{-1}$), (d) ice density ($kg \cdot m^{-3}$), (e) air bubble effective radius (μm) and (f)
346 volume fraction of air in the period of 2000-2020.

347

348 After acquisition of the daily ice density and air bubble effective radius of the GrIS (Figs. 4d
349 and 4e), we again employed the standalone SNICAR-ADv4 model to simulate the NIR and
350 visible albedo for each bare ice grid cell of the GrIS. Using an iterative optimization approach,
351 we derived the equivalent BC concentration by adjusting the BC input parameter in the
352 standalone SNICAR-ADv4 until its simulated visible albedo matched the MODIS MCD43C3

删除[o_0 [2]]: 3
删除[o_0 [2]]: 3
删除[o_0 [2]]: R3
删除[o_0 [2]]: 2

observations. This inversion method relies on the strong influence of LACs on visible albedo and their negligible impact on NIR albedo over bare ice (Schneider et al., 2019). As seen in Figs. 5a-c, there is minimal difference in the albedo in the NIR band, with a slight underestimation of 0.029 by the standalone SNICAR-ADv4. In contrast, the SNICAR-ADv4 significantly overestimated the visible albedo by up to 0.293 when using these bare ice properties, as it did not account for the LACs (Figs. 5d-f). We incrementally adjusted the input BC concentration in the standalone SNICAR model to match the visible albedo values from MCD43C3 data at each GrIS bare ice grid cell (Figs. 5h and i). This process yielded the daily equivalent BC concentrations shown in Fig. 5g. Based on the MODIS data and the standalone SNICAR-ADv4 lookup table, the daily 0.5-deg ice density, air bubble effective radius and equivalent BC data were then processed into monthly timescale as input for CoLM. Besides, it is worth mentioning that not all bare ice grid cells are informed by the bare ice physical properties data in each summer month. These grid cells are filled with the climatological mean values of bare ice physical properties when retrievals fail due to clouds or poor data quality.

删除[o_0 [2]]: 4

删除[o_0 [2]]: 3

删除[o_0 [2]]: 4

删除[o_0 [2]]: 4

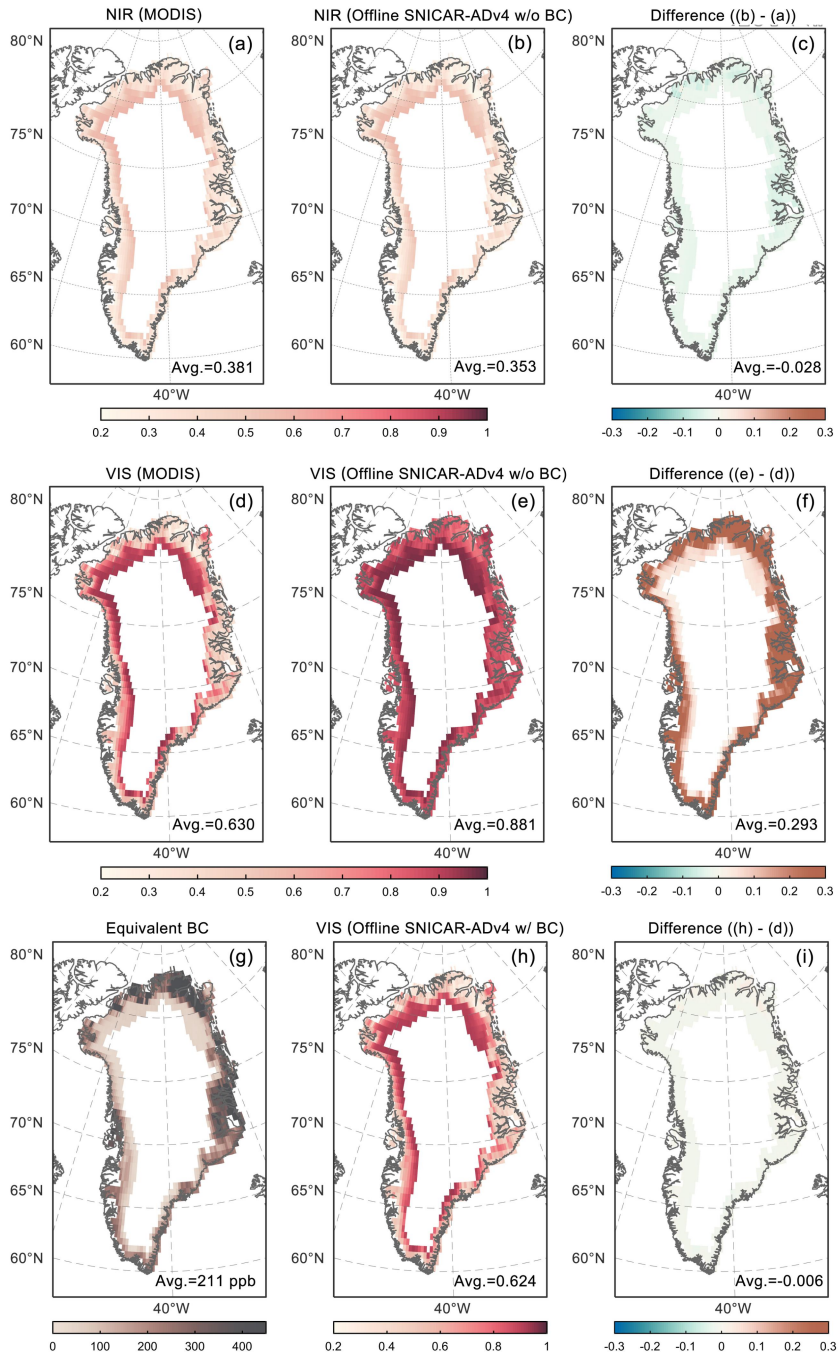

368

369 **Figure 5.** The spatial distributions of MODIS bare ice albedo and standalone SNICAR-ADv4

370 bare ice albedo excluding LACs in (a, b) near-infrared and (c, d) visible bands for JJA from

371 2000 to 2020, along with (c, f) their differences. The spatial distributions of (g) equivalent

372 black carbon, (h) the standalone SNICAR-ADv4 bare ice visible albedo with equivalent black

373 carbon (ppb), and (i) its difference from the MODIS bare ice visible albedo.

374

删除[o_0 [2]]: **4**

删除[o_0]: the

删除[o_0 [2]]:
We use the standalone SNICAR-ADv4 and briefly examine aforementioned factors influencing spectral albedo of ice with direct light conditions, including the SZA, ice density, air bubble effective radius (R_{eff}), and equivalent BC. As show ...

2.5 Model simulation

We conduct several offline CoLM simulations with the embedded SNICAR-ADv4 and SNICAR-AD schemes on a 0.25×0.25-degree resolution, driven by the atmospheric forcing from the hourly single-level surface dataset of the European Center for Medium-Range Weather Forecasts' fifth-generation atmospheric Reanalysis (ERA5) in the GrIS. Compared with other atmospheric forcings, ERA5's precipitation rates exhibit a higher correlation with measured net accumulation over the GrIS (Schneider et al., 2023). We run the model simulations for the years 1980–2020 and the summer melt season (June, July and August; JJA) during 2000-2020 is used for analysis. Aerosol concentration in the snow layer is calculated based on the prescribed monthly aerosol (BC, dust, OC) wet and dry deposition flux from the CESM2-WACCM simulations in CMIP6 experiments (Danabasoglu et al., 2020). The monthly bare ice properties for ice radiative transfer process are inferred from MODIS products using the standalone SNICAR-ADv4 over the bare ice region of the GrIS, covering JJA from 2000 to 2020, as the MODIS products has been available since 2000. To prevent possible unusual model behavior when shifting bare ice albedo schemes, the bare ice properties from the summer of 2000 were used in a brief spin-up run for the variable bare ice conditions in our experimental runs from 1998 to 2000. For land ice patches informed by the ice properties, the bare ice albedo is first calculated and replaces the constant values (0.6 for VIS and 0.4 for NIR). If snow is present over the ice, the new ice albedo of underlying ice column is used as the lower boundary to calculate snow albedo. The total patch albedo is then determined by the fractional coverage of land types and snow cover.

删除[o_0 [2]]: 5

删除[o_0 [2]]: 5

删除[o_0 [2]]: 6-

删除[o_0 [2]]: s

删除[o_0]: participated

删除[o_0]: the

In this study, we analyzed output variables from three sets of CoLM simulations: (1) those using SNICAR-AD with fixed bare ice albedo (0.6 for visible and 0.4 for near-infrared), (2) those using SNICAR-ADv4 with annually-varying bare ice properties and (3) those using SNICAR-ADv4 with bare ice properties held constant at year 2000 values for all years. The simulations output two variable groups: (a) surface albedo (visible, near-infrared, and shortwave under direct radiation) and bare ice fraction for albedo evaluation; (b) 2-m temperature, snow cover fraction, and snow water equivalent to quantify the effect from the

bare ice metamorphism.

3. Results

3.1 Mapping of GrIS bare ice physical properties

Figures 4c-f display the spatial distribution of summer climatological mean of the bare ice physical properties, including SSA, ice density, air bubble effective radius and volume fraction of air. The bare ice density gradually decreases from the lower-elevation coastal regions toward the interior, while the volume fraction of air shows an opposite pattern, as it is calculated from the bulk ice-air mixture density and the density of pure ice (Figs. 4d and f; Eqs. 1 and 2). SSA represents the total surface area of ice-air interfaces relative to the mass of ice, determined by the volume fraction of air, effective diameter of air bubbles, and the bulk density of the ice layer (Whicker-Clarke et al., 2022), with high values distributed in the area along the mean equilibrium line (Fig. 4b). Given the large discrepancy in bare ice visible albedo between the standalone SNICAR-ADv4 without LACs and the MCD43C3 in the coastal regions of the GrIS (Figs. 5d and e), higher equivalent BC concentrations occur in these areas compared to inland regions, indicating potentially more severe contamination, particularly in the southeastern and northernmost parts of the GrIS (Fig. 5g)..

3.2 Spatial and Temporal performance of CoLM Simulations

In this study, the "land ice" area (Fig. 6a) refers specifically to glacier ice grid cells excluding those persistently covered by snow. Therefore, interior regions of the GrIS, which are continuously overlain by permanent snow cover, are not counted as "land ice" in this figure. This explains the absence of land ice coverage in the GrIS interior. The land ice fraction in Fig. 6a represents the proportion of glacier ice within a grid cell after filtering out areas where snow cover fraction remains at 100%. Grid cells with land ice fraction < 1 contain a mix of glacier ice and other surface types (e.g., bare soil). In contrast, Fig. 6b shows the exposed bare ice fraction, which further considers seasonal snow cover using the SNICAR-AD scheme. It is important to note that, despite a slight difference in snow cover

删除[o_0 [2]]: 3

删除[o_0 [2]]: b

删除[o_0 [2]]: e

删除[o_0 [2]]: The bare ice density gradually decreases from the lower-elevation coastal regions toward the interior, while the volume fraction of air show an opposite pattern for it is calculated by bulk ice-air mixture density and pure ice density (Figs. 3c and e).

删除[o_0]: -

删除[o_0]: area

删除[o_0 [2]]: 3

删除[o_0 [2]]: 4

删除[o_0 [2]]: 3

删除[o_0 [2]]: The bare ice region of the GrIS in this study is defined as grid cells with exposed glacier ice (snow cover fraction <100%), where surface albedo is controlled by ice properties but also influenced by residual snow and bare soil patches. Figure 6a shows the spatial distribution of land ice underlying the snowpack. The areas where land ice is the main type of land cover are located in the periphery of the the GrIS with the exception of the southeastern edge. Values of land ice fraction below 1 implies that the corresponding grid cells contain other land cover type, e.g. bare soil. The exposed bare ice fraction (Fig. 6b) is calculated accounting for the snow coverage in each grid cell, utilizing the SNICAR-AD scheme.

fraction simulations, the choice of snow albedo scheme does not affect the selection of bare ice regions. The frequency distribution of the exposed bare ice fraction is shown in Fig. 6c. The bare ice fraction ranges from 0 to 0.7 across the grid cells, with the majority of grid cells exhibiting a bare ice fraction below 0.5. The histogram bars represent the relative proportion of grid cells within each bare ice fraction interval.

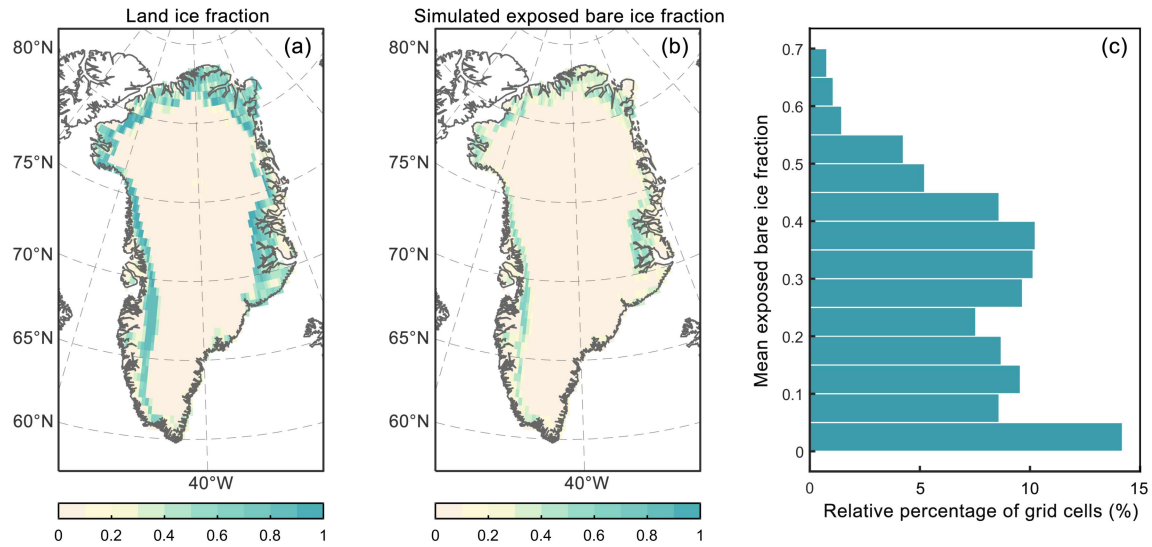

Figure 6. Spatial distribution of (a) the fraction of land ice underlying the snowpack, excluding interior regions of the GrIS that remain fully snow-covered throughout JJA (2000–2020), and (b) the mean exposed bare ice fraction during JJA over the same period, based on snow cover simulated by CoLM using the SNICAR-ADv4 scheme. Panel (c) shows the relative frequency distribution of mean exposed bare ice fraction, considering only grid cells with nonzero bare ice exposure. Each bar indicates the percentage of these grid cells whose mean bare ice fraction falls within a given interval, relative to the total number of bare ice grid cells.

To assess whether the integration of an ice radiative transfer solver in CoLM improves albedo simulations, we compared simulated albedo with the MCD43C3 albedo in shortwave, visible and NIR regions of the spectrum during the summer of 2000-2020 in bare ice region (Fig. 7). Both SNICAR-AD and SNICAR-ADv4 simulations use the same default snow albedo configuration, which includes spherical snow grains, the adding-doubling radiative transfer solver, and external mixing of BC/dust with snow. In other words, the differences in

删除[o_0 [2]]: The exposed bare ice fraction frequency distribution is shown in Fig. 6c, in which the bare ice fraction spans from 0 to 0.7, and in most areas, the bare ice fraction is less than 0.5.

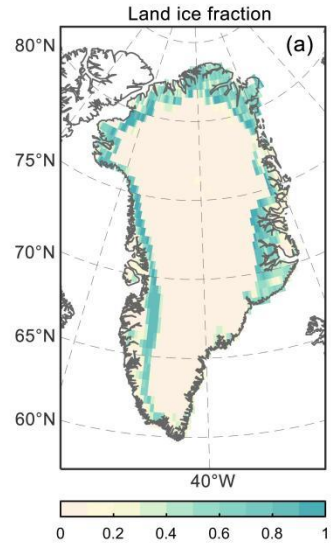

删除[o_0 [2]]:

删除[o_0 [2]]: Spatial distribution of (a) the fraction of land ice underlying snowpack and (b) exposed bare ice considering the snow cover simulated by CoLM SNICAR-ADv4 for the JJA from 2000 to 2020. (c) Frequency distribution of exposed bare ice within the bare ice region (excluding grid cells with no exposed bare ice), calculated as the proportion of grid cells within each bare ice fraction interval relative to the total number of bare ice grid cells.

删除[o_0 [2]]: Both schemes of SNICAR-AD and SNICAR-ADv4 maintain consistent settings for default snow albedo scheme, with sphere snow grain shape, adding-doubling radiative transfer solver, and BC/dust-snow external mixing state.

simulated albedo between SNICAR-AD and SNICAR-ADv4 arise solely from their different treatments of ice albedo, as the snow albedo configuration remains identical. As seen in Figs. 7a-c, it is obvious that the SNICAR-AD enabled CoLM albedo is significantly overestimated across all bare ice regions, by 0.086 in shortwave, 0.078 in visible and 0.095 in NIR. Compared with CoLM SNICAR-AD, the application of the SNICAR-ADv4 scheme reduced the overestimation of albedo for all bands, by 38% in the shortwave, 50% in the visible and 28% in the NIR (Figs. 7d-f).

Furthermore, for each grid cell over the GrIS bare ice region, we computed the root-mean-square error (RMSE) between the MODIS observed albedo and model-simulated albedo (CoLM-SNICAR-AD/SNICAR-ADv4) time series (2000-2020, 21 summer values per cell). Comparative analysis of the spatial distributions of correlation coefficients, RMSE, and linear trends (Figs. S1-S3) reveals that CoLM-SNICAR-ADv4 outperforms CoLM-SNICAR-AD across all evaluation metrics. These metrics were derived by comparing the 21-year summer albedo time series from model simulations and MODIS observations at each grid cell: correlation coefficients evaluate the phase similarity of interannual variations, RMSE quantifies deviation magnitudes, and linear trends (obtained via least-squares regression) capture interannual albedo changes. The comprehensive spatial evaluation demonstrates consistent improvements in both the spatial pattern and quantitative representation.

删除[o_0 [2]]: In other words, the differences in albedo simulated by these two schemes are determined by the treatment for ice albedo.

删除[o_0 [2]]: d

删除[o_0 [2]]: f

删除[o_0 [2]]: i

删除[o_0 [2]]: Furthermore, comparative analysis of the spatial distributions of correlation coefficients, root mean square errors (RMSE), and linear trends (Figs. S1-S3) reveals that CoLM-SNICAR-ADv4 outperforms CoLM-SNICAR-AD across all evaluation metrics. These metrics were derived from each grid cell by comparing the 21-year summer albedo time series (2000-2020) from model simulations and MODIS observations: correlation coefficients assess temporal agreement, RMSE quantifies deviation magnitudes, and linear trends (obtained via least-squares regression) capture interannual albedo changes. The comprehensive spatial evaluation demonstrates consistent improvements in both the spatial pattern and quantitative representation.

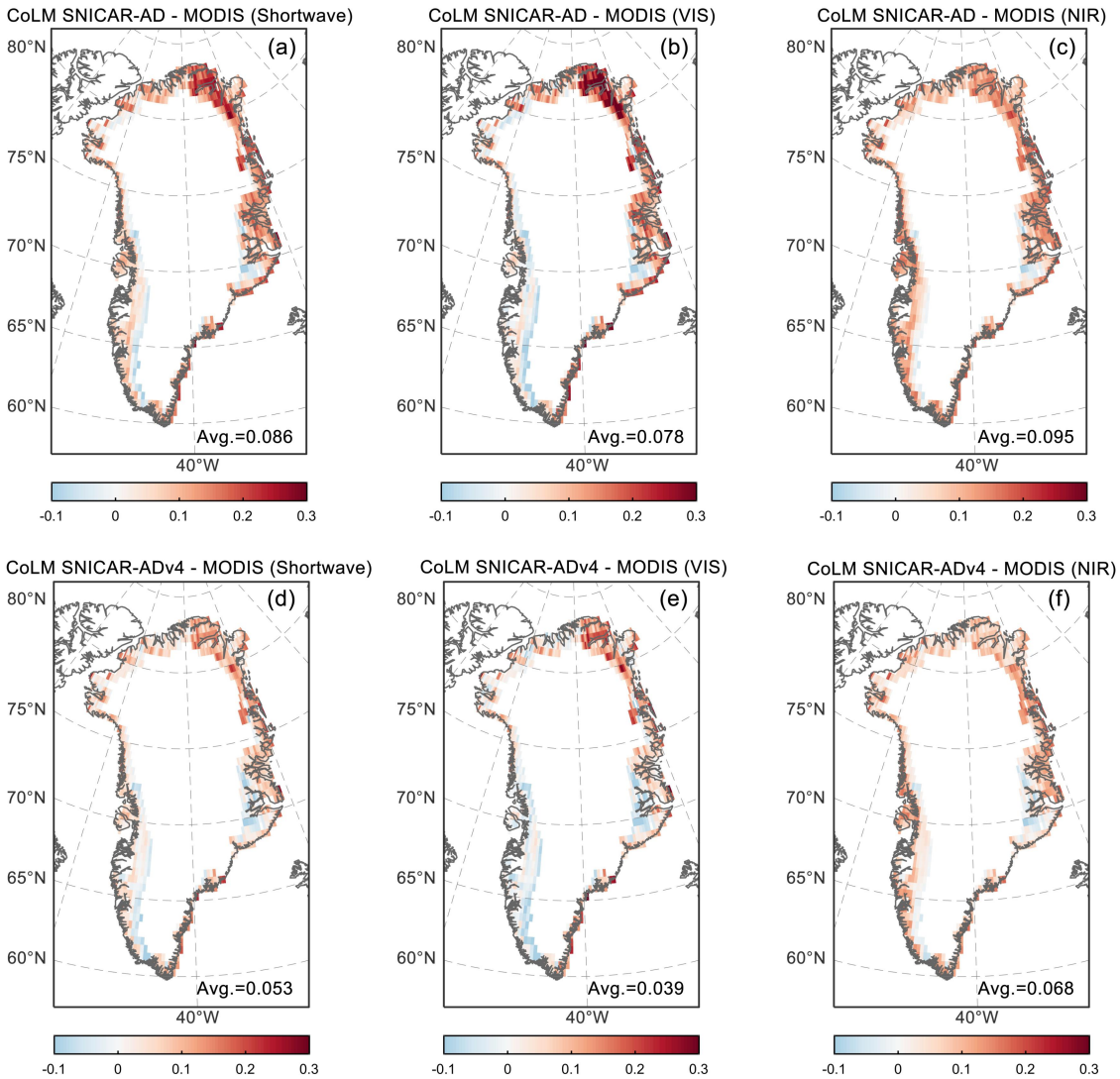

Figure 7. Spatial distribution of the difference of the 2000-2020 JJA albedo between the CoLM with different snow/ice albedo schemes (SNICAR-AD and SNICAR-ADv4) and the MCD43C3 in the (a, d) shortwave (0.3–5.0 μm), (b, e) visible (0.3–0.7 μm) and (c, f) near-infrared (0.7–5.0 μm) bands.

The decrease in the positive bias of CoLM SNICAR-ADv4 can also be clearly seen in the shortwave, visible and near-infrared albedo time series, with the area-weighted mean albedo of the GrIS bare ice regions steadily decreasing throughout the summer period from 2000 to 2020, compared with CoLM SNICAR-AD (Fig. 8). The albedo of CoLM SNICAR-ADv4 fluctuates around 0.47 in the shortwave, 0.53 in the visible, and 0.4 in the NIR, which is approximately 0.05 higher than the corresponding values in MCD43C3. In addition, the

CoLM SNICAR-ADv4 simulations exhibit synchronous variations in albedo with those of MCD43C3, and there are relatively high temporal correlations between the CoLM SNICAR-ADv4 and MCD43C4 albedo, with the values up to 0.95 for the shortwave, visible, and NIR bands. In contrast, the albedo from the CoLM SNICAR-AD shows lower correlation with MCD43C3 due to its constant ice albedo treatment. It is obvious that a large interannual variability in the SNICAR-ADv4 enabled CoLM albedo is consistent with that of the MCD43C3, while the simulated albedo using SNICAR-AD scheme presents a weaker interannual variability. Regarding correlation with observations, SNICAR-AD achieves slightly lower correlation (0.91) in the NIR band compared to its performance in the shortwave and visible bands (both 0.92).

删除[o_0]: in consistence

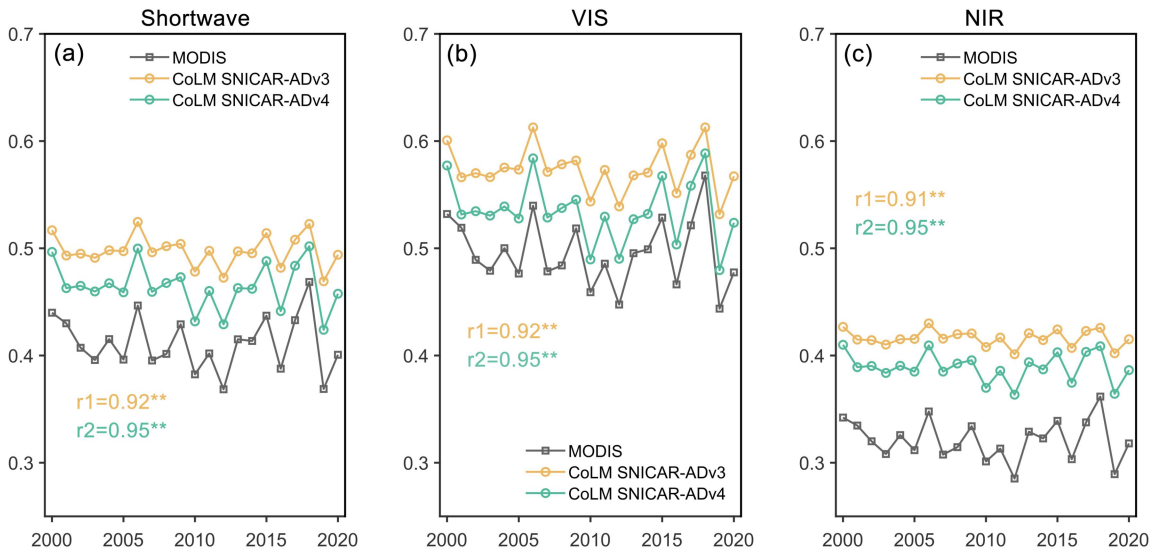

Figure 8. Time series of the 2000-2020 JJA CoLM SNICAR-AD and SNICAR-ADv4 albedo versus the MCD43C3 albedo over bare ice region, in the (a) shortwave (0.3–5.0 μm), (b) visible (0.3–0.7 μm) and (c) near-infrared (0.7–5.0 μm) bands. Double asterisks indicates significance at the 99% confidence level.

Given that the bias reduction varies across regions with different bare ice coverages, we explore the distribution of the albedo from CoLM SNICAR-AD, CoLM SNICAR-ADv4 and MCD43C3 under different bare ice fractions. Generally, as bare ice fraction increases, CoLM SNICAR-ADv4 can more effectively reduce the overestimation of shortwave broadband

albedo (BBA) compared to CoLM SNICAR-AD, due to its improved simulation of bare ice BBA (Fig. 9). For regions where bare ice covers more than half the area, the albedo overestimation of SNICAR-AD was reduced significantly by up to 99%. When the bare ice fraction is between 0.4 and 0.5, the percentage of overestimation reduction in albedo decreases to 74%, followed by regions with bare ice fraction of 0.3-0.4 (52%), 0.2-0.3 (38%), 0.1-0.2 (25%), and 0-0.1 (10%), respectively.

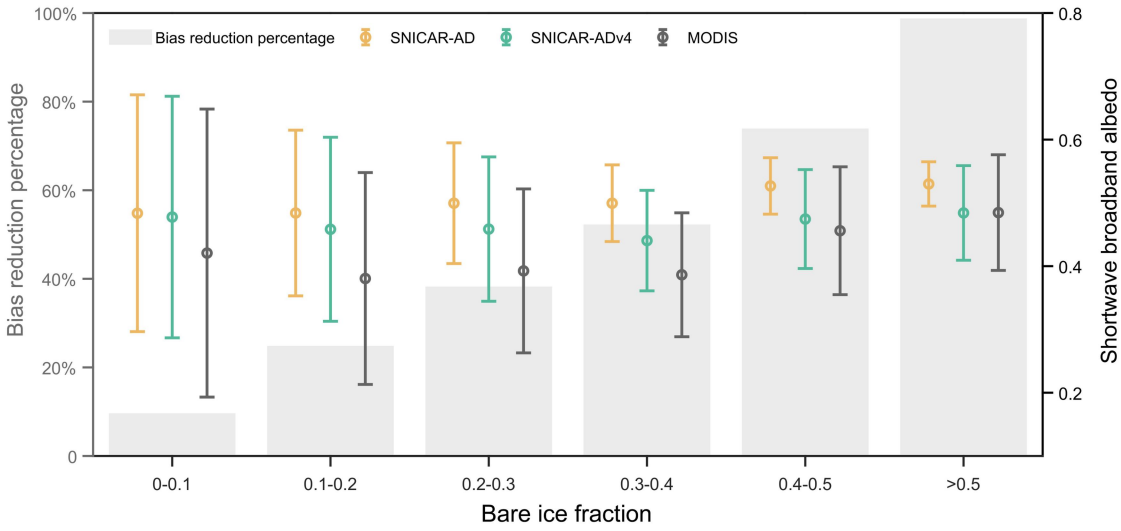

Figure 9. Mean shortwave broadband albedo from CoLM SNICAR-AD, CoLM SNICAR-ADv4 and MCD43C3 under different bare ice fractions (error plots). The uncertainty is calculated as double standard error, which reflects the 95% confidence interval. The percentages of CoLM SNICAR-ADv4 albedo reduction in bias are represented by grey bars.

3.3 A feedback revealed by bare ice property changes

删除[o_0]: **properties change**

The application of the SNICAR-ADv4 scheme in CoLM has significantly reduced the bias in albedo simulations. To investigate the regional climatic response to bare ice metamorphism of Greenland's bare ice region, we conduct a simulation in which the bare ice physical properties for each year are set to the values from 2000. By calculating the difference in simulated albedo between the simulations with annually varying bare ice properties and those

using the 2000 values, the model sensitivities to the change in summer bare ice albedo can be assessed to quantify its impact on 2-m temperature and snow cover. To better highlight the impact of changes in bare ice physical properties, the study area was restricted to regions with a bare ice fraction larger than 0.4. Figures 10a-c compares the effects of bare ice metamorphism on the 21-year summer mean albedo, 2-m temperature and snow cover fraction, between simulations with annually varying bare ice properties and those using constant year-2000 properties. The regional weighted mean albedo difference between the two experiments reaches 0.032, indicating that the albedo in the bare ice region is reduced by 0.032 during the summer due to bare ice metamorphism (Fig. 10a). This leads to a 0.071°C 2-meter temperature forcing and a -0.011 change in snow cover fraction over the study period (Figs. 10b and c). These results suggest that the temperature increase associated with the change in albedo contributes to snow melting.

Spatially, the regions with strong response of near surface air temperature to bare ice albedo changes are concentrated in the edge of the northwestern and western ablation zones, where the 2-temperature increased by over 0.1°C in most part of these areas (Fig. 10b). A similar response pattern can be also seen in the difference distribution of the snow cover (Fig. 10c), with decrease in snow cover fraction exceeding 0.04 in parts of the northwestern and western GrIS where temperature increases are most pronounced. To further evaluate the hydrological implications of albedo-induced warming, we examined changes in snow water equivalent, which integrates snow accumulation, meltwater retention, and sublimation processes. This analysis indicates that bare ice metamorphism represented by annually varying ice properties leads to a forcing that causes an average snow water equivalent decrease of 1.345 mm (Fig. 10d), consistent with the observed snow cover decline. The statistical distributions of changes in 2-m temperature, snow cover, and snow water equivalent (Fig. 10e) reinforce the finding that certain regions of the GrIS are especially sensitive to reductions in bare ice albedo. Although the mean differences in 2-m air temperature, snow cover, and snow water equivalent appear small, there are a considerable number of grid cells showing substantially higher 2-m air temperature differences and notably lower snow cover and snow water equivalent values. This indicates that certain regions of the GrIS exhibit relatively strong

554 sensitivity to changes in bare ice albedo (Fig. 10e). These coordinated changes manifest a
555 strong bare ice-albedo feedback in the GrIS bare ice region because bare ice albedo is
556 reduced through physical and biological melt-albedo processes that darken the ice surface as
557 the warming occurs in the ice surface.
558
559 The metamorphism of bare ice could be manifested in the changes in ice density and air
560 bubble radius with the ice, and these two factors jointly determine the specific surface area
561 (Eq.1) which have a one-to-one relationship with the bare ice albedo (Fig. 3b). From Fig. 10f,
562 the difference in BBA shows a strong positive correlation with the specific surface area, with
563 a correlation coefficient of 0.88 (significant at the 99% confidence level), since the two
564 simulations differ solely in their bare ice physical property inputs to the land surface model.
565 As more intense melt processes start in the early summer of the GrIS ablation zone after 2000,
566 the lower specific surface area, linked with the bare ice-albedo feedback, consistently
567 contributes to the reduction of the BBA (Fig. 10f). Additionally, according to the sensitivity
568 of modeled spectral albedo to the relevant parameters of the standalone SNICAR-ADv4
569 model (Fig. 5), the decreased bare ice albedo, associated with a lower specific surface area,
570 suggests an overall increase in ice density and a larger size of air bubbles within the ice in the
571 GrIS bare ice region.

删除[o_0]: the

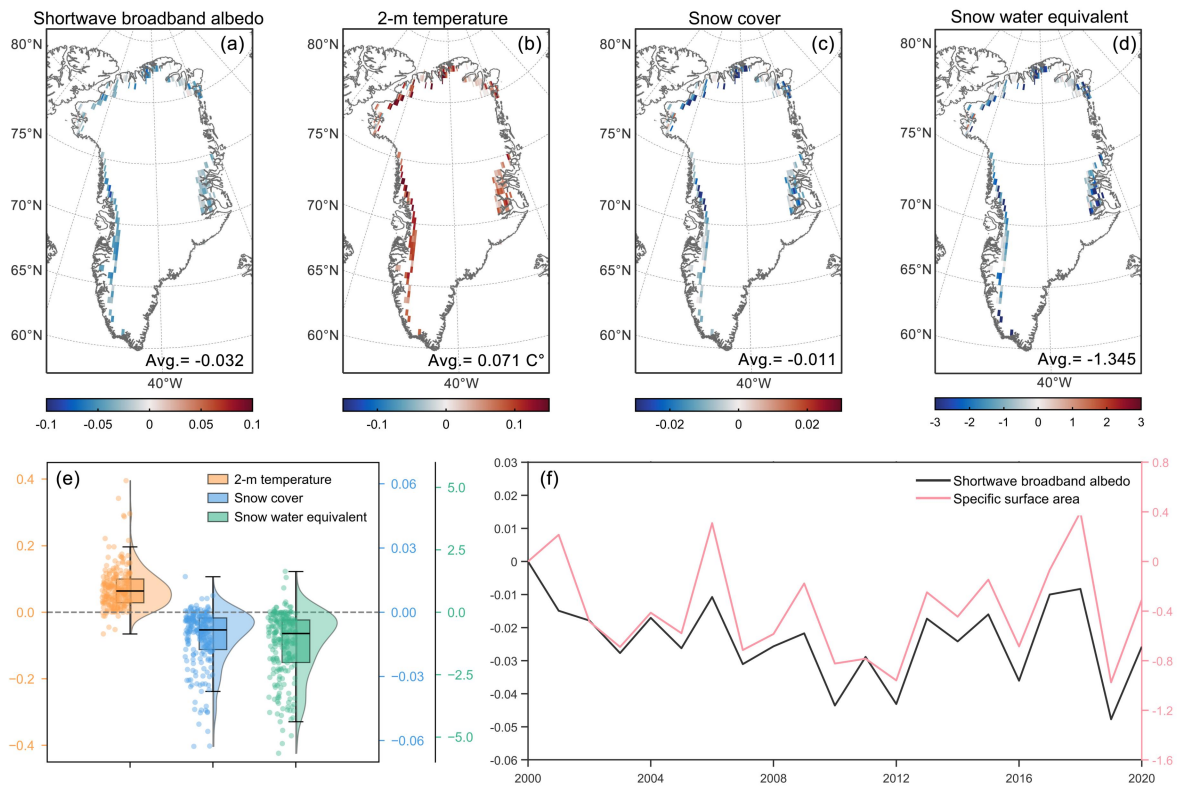

572

573 **Figure 10.** Spatial differences between simulations using annually varying bare ice properties

574 and those using fixed year-2000 values during JJA (June–August) from 2000 to 2020: (a)
575 surface albedo, (b) 2-m air temperature (°C), (c) snow cover fraction, and (d) snow water
576 equivalent (mm). (e) Statistical distributions of differences in 2-m air temperature, snow
577 cover, and snow water equivalent, shown using combined boxplots, left-side jittered points,
578 and right-side half-violin plots. (f) Time series of differences in specific surface area ($m^2 \cdot kg^{-1}$)
579 and simulated shortwave broadband albedo between the two experiments.
580
581 After 2000, the metamorphism of bare ice in the Greenland bare ice region is mainly reflected
582 in the decrease of SSA, which leads to ice darkening. This, in turn, induces regional
583 near-surface temperature increases, causing snowmelt and ultimately resulting in a reduction
584 of snow cover. Changes in snow cover directly determine the extent of bare ice exposure and
585 significantly affect the albedo through snow-albedo feedback. The obvious snow cover
586 reduction attributed to the changes in the physical properties of bare ice will cause more dark
587 ice exposure and darkening, and make a constant contribution to albedo reduction in this
588 ablation zone, suggesting a potential linkage between the bare ice-albedo and the

删除[o_0 [2]]: contraction

snow-albedo feedback.

4. Conclusions and Discussion

In this study, we incorporated SNICAR-ADv4 into the CoLM and made an enhanced MODIS-informed bare ice physical properties to explore the response of the bare ice albedo to ice metamorphism under polar warming. The application of SNICAR-ADv4, together with the integration of MODIS-derived bare ice properties, significantly improved albedo simulations by reducing the bias introduced by the default constant ice albedo treatment. Specifically, bias reductions of 38%, 50%, and 28% were achieved for broadband, visible, and near-infrared albedo, respectively. This improvement stems not only from the physically enhanced radiative transfer calculations over the ice column in SNICAR-ADv4, but also from the critical incorporation of MODIS-constrained ice optical properties, such as ice density and bubble radius. These additions provide better physical realism and representation of surface conditions across the bare ice zone. The snow and ice treatment used in CoLM SNICAR-ADv4 and SNICAR-AD schemes are summarized in the Fig. 1, and it is evident that SNICAR-ADv4 performs radiative transfer calculations not only over the snow column but also over the ice column. During the summertime of 2000-2020, the bare ice BBA decreased by 0.032 due to the changes in bare ice physical properties. The subsequent darkening of the bare ice led to a 2-m air temperature forcing of 0.071°C, a change in snow cover of -0.011 and snow water equivalent of -1.345 mm over the 21-year period, suggesting that even a slight reduction in bare ice albedo can produce measurable climate responses in the ablation region.

Our results are consistent with, and extend, recent progress in modeling bare ice albedo modeling over the GrIS. Antwerpen et al. (2022) demonstrated that the regional MAR model overestimated bare ice albedo by 22.8% below 70°N, leading to significant underestimation of meltwater production. Similarly, Wicker-Clarke et al. (2024) found that the global ELM-E3SM model overestimated shortwave broadband albedo by ~5% due to the use of fixed albedo parameters, and showed that incorporating more realistic bare ice albedo

删除[o_0]: the

删除[o_0]: The use of SNICAR-ADv4 in CoLM significantly reduces the severe overestimation originated from the default ice albedo treatment, with the improvement of the albedo modeling by 38%, 50% and 28% for the BBA, visible and NIR albedo.

删除[o_0]: SNICAR-ADv4 schemes, and SNICAR-AD

删除[o_0 [2]]: noticeable

reduced the SMB by approximately 145 Gt between 2000 and 2021. Although both studies focus on the GrIS, they differ in model structure and spatial resolution: MAR is a high-resolution regional climate model, while ELM-E3SM is part of a coarser-resolution global Earth system model. Despite these differences, both studies highlight a persistent bias-systematic overestimation of bare ice albedo. The convergence of evidence from diverse modeling frameworks underscores the need to improve bare ice representation in land surface models. Building on these insights, our study examines the role of bare ice metamorphism, particularly changes in specific surface area, in driving progressive surface darkening. By isolating the feedback between evolving ice properties and surface energy balance, we propose a physical mechanism for the observed albedo decline. Our sensitivity analysis underscores how bare ice metamorphism can influence surface energy balance and the importance of incorporating such processes in future model developments.

删除[o_0 [2]]: surface mass balance

删除[o_0]: ly

Our findings also highlight the role of the bare ice-albedo feedback linked to changes in ice surface properties, as shown in Fig. 11. A marked reduction in snow cover occurred due to lowered albedo in the ablation zone, exposing more bare ice and further reducing regional albedo, especially in northern GrIS. This agrees with previous findings that increased bare ice exposure has intensified the snow-albedo feedback in this region, with its strength rising by 51% from 2001 to 2017 (Ryan et al., 2019). The physical processes governing snowpack evolution play a crucial role in modulating surface albedo and associated feedbacks, particularly in the ablation zone of the GrIS, where snow loss accelerates bare ice exposure and amplifies radiative forcing. More specifically, new snow quickly loses reflectivity through grain growth and vapor diffusion, with subsequent changes driven by temperature gradients and compaction (Flanner and Zender, 2006). Meltwater accelerates these processes through melt-refreeze cycles (Brun 1989), creating a self-reinforcing system where both ice exposure and snow aging enhance surface darkening. While biological and hydrological factors such as algal growth play a secondary role in ice darkening (Ryan et al., 2019), our results demonstrate that changes in bare ice properties, particularly a downward trend in specific surface area at a rate of -0.007 yr^{-1}, exert a significant control over meltwater production. We collectively term these processes of the variation in the bare ice albedo

associated with snow melting the bare ice-snow-albedo feedback (Fig. 11). As rising temperatures may further reduce ice albedo, this feedback could substantially increase Greenland's contribution to sea level rise through enhanced melting (Ryan et al., 2019), highlighting the need for improved process understanding in climate projections.

This study advances our understanding of the performances of the GrIS's snow and ice albedo simulations using different snow/ice schemes (SNICAR-AD and SNCIAR-ADv4), and the amplifying effect of bare ice on the albedo reduction through bare ice-snow-feedback mechanism. However, three key limitations constrain our current findings. First, the 0.5°×0.5° resolution is insufficient to accurately represent the narrow ablation zone, and big resolution gap between MODIS data and the model output is a limitation of this study. Second, CoLM's representation of GrIS glaciers prescribed fixed ice thickness and mass with internally retained meltwater prevents calculation of SMB, and excludes ice melt contributions to runoff. Although computationally efficient, this simplification systematically underestimates meltwater export from Greenland's ablation zones, where surface processes and especially meltwater runoff are the dominant contributors to mass loss (Ryan et al., 2019, van den Broeke et al., 2016, The IMBIE Team, 2020). Third, methodological constraints prevent independent quantification of ice density and air bubble size effects, as their relationship is prescribed in the lookup table (ρ_{ice}=650 kg·m^{-3} corresponds to R_{eff}=100 μm, ρ_{ice}=916 kg·m^{-3} corresponds to R_{eff}=1500 μm) based on the standalone SNICAR-ADv4 model. Future work will address these limitations by employing higher-resolution modeling for more precise delineation of bare ice margins, improving the representation of surface mass balance and ice-melt runoff through a more complete physically based snow and ice surface scheme, and establishing observational constraints on ice density and air bubble effective radius evolution to enhance ice albedo modeling. Future efforts are also needed to consider the actual LACs concentrations within the ice, including BC, dust and snow algae, rather than relying on equivalent BC, and evaluate their impacts on GrIS mass loss using fully coupled land-atmosphere models, which may reveal more pronounced feedbacks than offline simulations.

删除[o_0 [2]]: surface mass balance

删除[o_0 [2]]: Although computationally efficient, this simplification systematically underestimates meltwater export from Greenland's ablation zones, where ice dynamical processes dominate mass loss.

删除[o_0 [2]]: Future work will address these limitations by employing higher-resolution modeling for more precise delineation of bare ice margins, coupling a dynamic ice sheet model to properly simulate the SMB and ice-melt runoff contributions, and establishing observational constraints on ice density and air bubble effective radius evolution to improve ice albedo modeling.

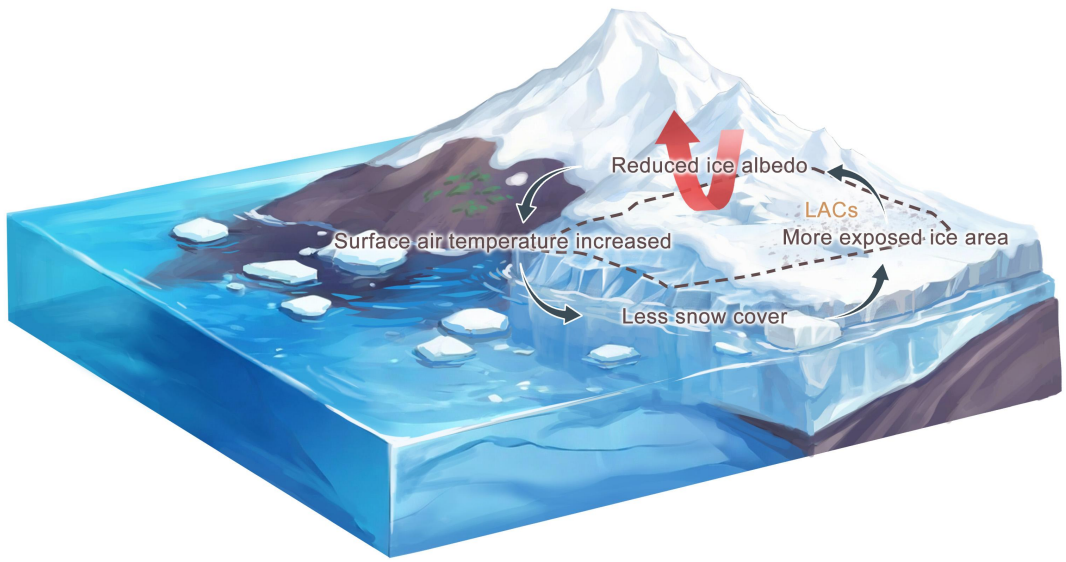

Figure 11. Illustration of the bare ice-snow-albedo feedback over the Greenland Ice Sheet. A reduction in ice albedo, primarily driven by changes in bare ice surface properties, exposes more bare ice, further lowering regional albedo and raising surface air temperatures. This leads to a decline in snow cover, which accelerates bare ice exposure and reinforces radiative forcing. This positive feedback loop intensifies melt, particularly in the ablation zone, contributing to increased surface darkening and meltwater production.

Data availability. The SNICAR-ADv4 enabled CoLM2024 code is available on GitHub at https://github.com/guoshuyang23/CoLM-SNICARADv4. The standalone SNICAR-ADv4 used in this study can be downloaded at https://github.com/chloewhicker/SNICAR-ADv4. MODIS snow cover data (MOD10C1) used to make the cloud and snow mask for bare ice pixels is available at https://nsidc.org/data/mod10c1/versions/6. MODIS surface reflectance data (MOD09CMG) used to retrieve the bare ice properties is from https://doi.org/10.5067/MODIS/MOD09CMG.061. MODIS surface albedo data (MCD43C3) used to evaluate the simulations and retrieve the bare ice properties is from https://doi.org/10.5067/MODIS/MCD43C3.061

Author contributions. SYG designed the study and wrote the paper. YJD was responsible for to conceptualization, supervision, and funding acquisition. HY contributed to revisions of the

manuscript. HBL provided technical support.

Competing interests. The contact author has declared that neither they nor their co-authors have any competing interests.

Acknowledgements. We thank Chloe A. Whicker-Clarke for sharing the method for processing ice optical property files in the standalone SNICAR-ADv4 for use in land surface models.

Financial support. This research was funded by the Guangdong Major Project of Basic and Applied Basic Research (2021B0301030007), the Natural Science Foundation of China (under Grants U2342227, 42075160, and 42088101), the Southern Marine Science and Engineering Guangdong Laboratory (Zhuhai) (No. SML2023SP216), and the specific research fund of the Innovation Platform for Academicians of Hainan Province (YSPTZX202143).

References

Abolafia-Rosenzweig, R., He, C., McKenzie Skiles, S., Chen, F., and Gochis, D.: Evaluation and optimization of snow albedo scheme in Noah-MP land surface model using in situ spectral observations in the Colorado Rockies, J. Adv. Model. Earth Syst., 14, e2022MS003141, https://doi. org/10.1029/2022MS003141, 2022.

Alexander, P. M., Tedesco, M., Fettweis, X., van de Wal, R. S. W., Smeets, C. J. P. P., and van den Broeke, M. R.: Assessing spatio-temporal variability and trends in modelled and measured Greenland ice sheet albedo (2000–2013), The Cryosphere, 8(6), 2293–2312, https://doi.org/10. 5194/tc-8-2293-2014, 2014.

Antwerpen, R., Tedesco, M., Fettweis, X., Alexander, P.,and vandeBerg, W. J.: Assessing bare-ice albedo simulated byMAR overthe Greenland icesheet(2000–2021) andimplications formeltwater production estimates, The Cryosphere, 16(10), 4185–4199, https://doi.org/10. 5194/tc-16-4185-2022, 2022.

Box, J. E., Fettweis, X., Stroeve, J. C., Tedesco, M., Hall, D. K., and Steffen, K.: Greenland ice sheet albedo feedback: Thermodynamics and atmospheric drivers, The Cryosphere, 6(4), 821–839, https://doi.org/10.5194/tc-6-821-2012, 2012.

Briegleb, B. P. and Light, B.: A Delta-Eddington multiple scattering parameterization for solar radiation in the sea ice component of the Community Climate System Model, NCAR/TN472+STR, National Center for Atmospheric Research, 108 pp., https://doi.org/10.5065/D6B27S71, 2007.

Brun, E.: Investigation of wet-snow metamorphism in respect of liquid-water content, Ann. Glaciol., 13, 22 – 26, https://doi.org/10.3189/S0260305500007635, 1989.

Chen, X., Zhang, X. , Church, J. A., Watson, C. S., King, M. A., Monselesan, D., Legresy, B., and Harig C.: The increasing rate of global mean sea-level rise during 1993-2014, Nat. Clim. Change,7, 492–495, https://doi.org/10.1038/nclimate3325, 2017.

Chevrollier, L. A., Cook, J. M., Halbach, L., Jakobsen, H., Benning, L. G., Anesio, A. M., and Tranter, M.: Light absorption and albedo reduction by pigmented microalgae on

741 snow and ice, J. Glaciol., 69(274), 333–341. https://doi.org/10.1017/jog.2022.64, 2023.

742 Cogley, J. G., Hock, R., Rasmussen, L. A., Arendt, A. A., Bauder, A., Braithwaite, R. J.,
743 Jansson, P., Kaser, G., Möller, M., Nicholson, L.: Glossary of glacier mass balance and
744 related terms (p. 86), IHP-VII Technical Documents in Hydrology No, 2011.

745 Cook, J. M., Tedstone, A. J., Williamson, C., McCutcheon, J., Hodson, A. J., Dayal, A.,
746 Skiles, M., Hofer, S., Bryant, R., McAree, O., McGonigle, A., Ryan, J., Anesio, A. M.,
747 Irvine-Fynn, T. D. L., Hubbard, A., Hanna, E., Flanner, M., Mayanna, S., Benning, L. G.,
748 van As, D., Yallop, M., McQuaid, J. B., Gribbin, T., and Tranter, M.: Glacier algae
749 accelerate melt rates on the south-western Greenland Ice Sheet, The Cryosphere, 14,
750 309330, https://doi.org/10.5194/tc-14-309-2020, 2020.

751 Danabasoglu, G., Lamarque, J. F., Bacmeister, J., Bailey, D. A., DuVivier, A. K., Edwards, J.,
752 Emmons, L. K., Fasullo, J. T., Garcia, R., Gettelman, A., Hannay, C., Holland, M. M.,
753 Large, W. G., Lauritzen, P., Lawrence, D. M., Lenaerts-Jan T. M., Lindsay, K.,
754 Lipscomb, W. H, Mills, M. J., Neale, R., Oleson, K., Otto-Bliesner, B., Phillips, A. S.,
755 Sacks, W. J., Tilmes, S., van Kampenhout, L., Vertenstein, M., Bertini, A., Dennis, J.,
756 Deser, C., Fischer, C., Fox-Kemper, B., Elizabeth-Kay, J., Kinnison, D., Kushner, P.,
757 Larson, V. E., Long, M., Mickelson, S., Moore, J. K., Nienhouse, E., Polvani, L., Rasch,
758 P. J., and Strand, W. G..: The community Earth system model version 2 (CESM2), J.
759 Adv. Model. Earth Syst., 12, https://doi.org/10.1029/2019MS001916, 2020.

760 Dang, C., Zender, C. S., and Flanner, M. G.: Intercomparison and improvement of
761 two-stream shortwave radiative transfer schemes in Earth system models for a unified
762 treatment of cryospheric surfaces, The Cryosphere, 13(9), 2325–2343.
763 https://doi.org/10.5194/tc-13-2325-2019, 2019.

764 Feng, S., Cook, J. M., Naegeli, K., Anesio, A. M., Benning, L. G., and Tranter, M.: The
765 impact of bare ice duration and geo-topographical factors on the darkening of the
766 Greenland Ice Sheet, Geophys. Res. Lett., 51, e2023GL104894, https://doi.
767 org/10.1029/2023GL104894, 2024.

768 Flanner, M. G., and Zender, C. S. Linking snowpack microphysics and albedo evolution, J.

Geophys. Res., 111(D12), https://doi.org/10.1029/2005JD006834, 2006.

Flanner, M. G., Arnheim, J. B., Cook, J. M., Dang, C., He, C., Huang, X., Singh, D., Skiles, S. M., Whicker, C. A., and Zender, C. S.: SNICAR-ADv3: a community tool for modeling spectral snow albedo, Geosci. Model Dev., 14, 7673 – 7704, https://doi.org/10.5194/gmd-14-7673-2021, 2021.

Flanner, M. G., Liu, X., Zhou, C., Penner, J. E., and Jiao, C.: Enhanced solar energy absorption by internally-mixed black carbon in snow grains, Atmos. Chem. Phys., 12(10), 4699–4721, https://doi.org/10.5194/acp-12-4699-2012, 2012.

Flanner, M. G., Zender, C. S., Randerson, J. T., and Rasch, P. J.: Present-day climate forcing and response from black carbon in snow. J. Geophys. Res., 112(D11). https://doi.org/10.1029/2006jd008003, 2007.

Friedl, M.A., Sulla-Menashe, D., Tan, B., Schneider, A., Ramankutty, N., Sibley, A., and Huang X.: Modis collection 5 global land cover: algorithm refinements and characterization of new datasets. Remote Sens. Environ, 114(1), 168–182, https://doi.org/10.1016/j.rse.2009.08.016, 2010

Gardner, A. S., and Sharp, M. J.: A review of snow and ice albedo and the development of a new physically based broadband albedo parameterization, J. Geophys. Res., 115(F1), F01009, https://doi.org/10.1029/2009JF001444, 2010.

Hao, D., Bisht, G., Rittger, K., Bair, E., He, C., Huang, H., Dang, C., Stillinger, T., Gu., Y., Wang, H., Qian, Y., Leung, L. R.: Improving snow albedo modeling in the E3SM land model (version 2.0) and assessing its impacts on snow and surface fluxes over the Tibetan Plateau, Geosci. Model Dev., 16(1), 75–94, https://doi.org/10.5194/gmd-16-75-2023, 2023.

He, C., and Flanner, M.: Snow albedo and radiative transfer: Theory, modeling, and parameterization. In Springer series in light scattering (pp. 67–133), Springer, 2020.

He, C., Flanner, M. G., Chen, F., Bariage, M., Liou, K. N., Kang, S., Ming, J., and Qian, Y.: Black carbon-induced snow albedo reduction over the Tibetan Plateau: Uncertainties

from snow grain shape and aerosol–snow mixing state based on an updated SNICAR model, Atmos. Chem. Phys., 18, 11507–11527, https://doi.org/10.5194/ACP-18-11507-2018, 2018.

He, C., Flanner, M., Lawrence, D. M., and Gu, Y.: New features and enhancements in community land model (CLM5) snow albedo modeling: Description, sensitivity, and evaluation, J. Adv. Model. Earth Syst., 16, e2023MS003861, https://doi. org/10.1029/2023MS003861, 2024.

He, C., Liou, K. N., Takano, Y., Chen, F., and Barlage, M.: Enhanced snow absorption and albedo reduction by dust-snow internal mixing: Modeling and parameterization, J. Adv. Model. Earth Syst., 11(11), 3755–3776, https://doi.org/10.1029/2019ms001737, 2019.

He, C., Takano, Y., Liou, K. N., Yang, P., Li, Q., and Chen, F.: Impact of snow grain shape and black carbon–snow internal mixing on snow optical properties: Parameterizations for climate models, Journal of Climate, 30(24), 10019–10036, https://doi.org/10.1175/jcli-d-17-0300.1, 2017.

Hofer, S., Tedstone, A. J., Fettweis, X. and Bamber, J. L.: Decreasing cloud cover drives the recent mass loss on the Greenland Ice Sheet, Sci. Adv., 3, e1700584, https://doi.org/10.1126/sciadv.1700584, 2017.

King, M. D., Howat, I. M., Candela, S. G., Noh, M. J., Jeong, S., Noël, B. P. Y., Van den Broeke, M. R., Wouters, B., and Negrete, A.: Dynamic ice loss from the Greenland Ice Sheet driven by sustained glacier retreat, Commun. Earth Environ., 1(1), 1. https://doi.org/10.1038/s43247-020-0001-2, 2020.

Kochtitzky, W., Copland, L., King, M., Hugonnet, R., Jiskoot, H., Morlighem, M., Millan, R., Khan, S. A., and Noël, B.: Closing Greenland's mass balance: Frontal ablation of every Greenlandic glacier from 2000 to 2020, Geophys. Res. Lett., 50, e2023GL104095, https://doi. org/10.1029/2023GL104095, 2023.

Li, Y., Yang, K., Gao, S., Smith, L.C., Fettweis, X., and Li, M.: Surface meltwater runoff routing through a coupled supraglacial-proglacial drainage system, Inglefield Land, northwest Greenland, Int. J. Appl. Earth. Obs, Geoinf, p. 106.

https://doi.org/10.1016/j.jprocont.2022.08.003, 2022.

Mouginot, J., Rignot, E., Bjørk, A. A., van den Broeke, M., Millan, R., Morlighem, M., Noël, B., Scheuchl, B., and Wood, M.: Forty-six years of Greenland Ice Sheet mass balance from 1972 to 2018, P. Natl. Acad. Sci., 116, 9239–9244, https://doi.org/10.1073/pnas.1904242116, 2019.

Müller, F. and Keeler, C. M.: Errors in short term ablation measurements on melting ice surfaces, J. Glaciol., 8(52), 91–105, 1969.

Mullen, P. C., and Warren, S. G.:. Theory of the optical properties of lake ice, J. Geophys. Res., 93(D7), 8403–8414, https:// doi.org/10.1029/JD093iD07p08403, 1988.

Naegeli, K., Damm, A., Huss, M., Wulf, H., Schaepman, M., and Hoelzle, M.: Cross-Comparison of albedo products for glacier surfaces derived from airborne and satellite (Sentinel-2 and Landsat 8) optical data, Remote Sens., 9(2), 110. https://doi.org/10.3390/ rs9020110, 2017.

Nolin, A.W., and Stroeve, J.: The changing albedo of the Greenland ice sheet: implications for climate modeling, Ann. Glaciol., 25, 51–57. https://doi. org/10.1017/s0260305500013793, 1997.

Picard, G., Libois, Q., and Arnaud, L.: Refinement of the ice ab-sorption spectrum in the visible using radiance profile measurements in Antarctic snow, The Cryosphere, 10(6), 2655–2672, https://doi.org/10.5194/tc-10-2655-2016, 2016

Ryan, J. C.: Contribution of surface and cloud radiative feedbacks to Greenland Ice Sheet meltwater production during 2002-2023, Commun. Earth Environ., 5(538), https://doi.org/10.1038/s43247-024-01714-y, 2024.

Ryan, J. C., Smith, L. C., van As, D., Cooley, S. W., Cooper, M. G., Pitcher, L. H., and Hubbard, A.: Greenland Ice Sheet surface melt amplified by snowline migration and bare ice exposure, Sci. Adv., 5(3), eaav3738, https://doi.org/10.1126/sciadv.aav3738, 2019.

Sasgen, I., Wouters, B., Gardner, A.S., King, M.D., Tedesco, M., Landerer, F.W., Dahle, C.,

Save, H., and Fettweis, X.: Return to rapid ice loss in Greenland and record loss in 2019 detected by the GRACE-FO satellites, Commun. Earth Environ, 1, 1-8. https://doi.org/10.1038/s43247-020-0010-1, 2020.

Schaaf, C., Wang, Z., and Strahler, A. H.: Commentary on Wang and Zender-MODIS snow albedo bias at high solar zenith angles relative to theory and to in situ observations in Greenland, Remote. Sens. Environ., 115, 1296 − 1300, https://doi.org/10.1016/j.rse.2011.01.002, 2011.

Schaaf, C., and Wang, Z.: MODIS/Terra+Aqua BRDF/Albedo Albedo Daily L3 Global 0.05Deg CMG V061 [Dataset]. NASA EOSDIS Land Processes DAAC, https://doi.org/10.5067/MODIS/MCD43C3.06, 2021.1

Schneider, A., Flanner, M., De Roo, R., and Adolph, A.: Monitoring of snow surface near-infrared bidirectional reflectance factors with added light-absorbing particles. The Cryosphere, 13(6), 1753–1766, https://doi.org/10.5194/tc-13-1753-2019, 2019

Schneider, A., Zender, C., Loeb, N., and Price, S.: Useofshallow icecoremeasurements toevaluate andconstrain 1980–1990 global reanalyses oficesheetprecipitation rates. Geophys. Res. Lett., 50(19), e2023GL103943, https://doi.org/10.1029/2023GL103943, 2023

Shimada, R., Takeuchi, N., and Aoki, T.: Inter-annual and geographical variations in the extent of bare ice and dark ice on the Greenland ice sheet derived from MODIS satellite images, Front Earth Sci., 4, 43, https://doi.org/10.3389/feart.2016.00043, 2016.

Stibal, M., Box, J. E., Cameron, K. A., Langen, P. L., Yallop, M. L., Mottram, R. H., Khan, A. L., Molotch, N. P., Chrismas, N. A. M., Quaglia, F. C., Remias, D., Smeets, P., Van den Broeke, M. R., and Ryan, J.: Algae drive enhanced darkening of bare ice on the Greenland ice sheet, Geophys. Res. Lett., 44(22), 11463–11471, https://doi.org/10.1002/2017GL075958, 2017.

Stroeve, J., Box, J. E., Gao, F., Liang, S., Nolin, A., and Schaaf, C.: Accuracy assessment of the MODIS 16-day albedo product for snow: Comparisons with Greenland in situ measurements, Remote. Sens. Environ., 94(1), 46–60.

https://doi.org/10.1016/j.rse.2004.09.001, 2005.

Tedesco, M., Doherty, S., Fettweis, X., Alexander, P., Jeyaratnam, J., and Stroeve, J.: The darkening of the Greenland ice sheet: Trends, drivers, and projections (1981–2100), The Cryosphere, 10(2), 477–496, https://doi.org/10.5194/tc-10-477-2016, 2016.

Tedstone, A. J., Cook, J. M., Williamson, C. J., Hofer, S., McCutcheon, J., Irvine-Fynn, T., Gribbin, T., and Tranter, M.: Algal growth and weathering crust state drive variability in western Greenland Ice Sheet ice albedo, The Cryosphere, 14, 521–538, https://doi.org/10.5194/tc-14-521-2020, 2020.

Tedstone, A. J., Bamber, J. L., Cook, J. M., Williamson, C. J., Fettweis, X., Hodson, A. J., and Tranter, M.: Dark ice dynamics of the south-west Greenland Ice Sheet, The Cryosphere, 11, 24912506, https://doi.org/10.5194/tc-11-2491-2017, 2017.

The IMBIE team: Mass balance of the Greenland ice sheet from 1992 to 2018, Nature, 579, 233-239, https://doi.org/10.1038/s41586-019-1855-2, 2020.

Toon, O. B., McKay, C. P., Ackerman, T. P., and Santhanam, K.: Rapid calculation of radiative heating rates and photodissocia-tion rates in inhomogeneous multiple scattering atmospheres, J. Geophys. Res., 94(D13), 16287–16301, https://doi.org/10.1029/ jd094id13p16287, 1989.

Urraca, R., Lanconelli, C., and Cappucci, F.: Gobron, N. Comparison of Long-Term Albedo Products against Spatially Representative Stations over Snow, Remote Sens., 14, 3745. https://doi.org/ 10.3390/rs14153745, 2022.

van den Broeke, Box, J., Fettweis, X., Hanna, E., Noël, B., Tedesco, M., van As, D., van de Berg, W. J., and van Kampenhout, L.: Greenland Ice Sheet Surface Mass Loss: Recent Developments in Observation and Modeling, Curr. Clim. Change Rep., 3, 345356, https://doi.org/10.1007/s40641-017-0084-8, 2017.

van den Broeke, M., Enderlin, E. M., Howat, I. M., Kuipers Munnneke, P., Noël, B. P. Y., van de Berg, W. J., van Meijgaard, E., Wouters, B.: On the recent contribution of the Greenland ice sheet to sea level change, The Cryosphere, 10, 1933-1946,

https://doi.org/10.5194/tc-10-1933-2016, 2016

Vermote, E.: MODIS/Terra Surface Reflectance Daily L3 Global 0.05Deg CMG V061 [Data set]. NASA EOSDIS Land Processes Distributed Active Archive Center, https://doi.org/10.5067/MODIS/MOD09CMG.061. 2021.

Warren, S. G., and Wiscombe, W. J.:. A model for the spectral albedo of snow. II: Snow containing atmospheric aerosols, J. Atmos. Sci., 37(12), 2734–2745, https://doi.org/10.1175/1520-0469(1980)037<2734:amftsa>2.0.co;2, 1980.

Whicker-Clarke, A., Antwerpen, R., Flanner, M. G., Schneider, A., Tedesco, M., and Zender, C. S.: The effect of physically based ice radiative processes on Greenland ice sheet albedo and surface mass balance in E3SM, J. Geophys. Res.-Atmos., 129, e2023JD040241, https://doi.org/10.1029/ 2023JD040241, 2024.

Whicker-Clarke, A., Flanner, M. G., Dang, C., Zender, C. S., Cook, J. M., and Gardner, A. S.: SNICAR-ADv4: A physically based radiative transfer model to represent the spectral albedo of glacier ice, The Cryosphere, 16(4), 1197–1220, https://doi.org/10.5194/tc-16-1197-2022, 2022.

Williamson, C. J., Anesio, A. M., Cook, J., Tedstone, A., Poniecka, E., Holland, A., Fagan, D., Tranter, M., and Yallop, M.: Ice algal bloom development on the surface of the Greenland Ice Sheet, FEMS Microbiol. Ecol., 94(3), https://doi.org/10.1093/femsec/fiy025, 2018.

Wiscombe, W. J., and Warren, S. G.: A model for the spectral albedo of snow. I: Pure snow. J. Atmos. Sci., 37(12), 2712–2733. https://doi.org/10.1175/1520-0469(1980)037<2712:amftsa>2.0.co;2, 1980.

Ye, F., Cheng, Q., Hao, W., Yu, D., Ma, C., Liang, D., and Shen, H.: Reconstructing daily snow and ice albedo series for Greenland by coupling spatiotemporal and physics-informed models, Int. J. Appl. Earth Obs., 124, 103519, https://doi.org/10.1016/j.jag.2023.103519, 2023.